remote sensing

MDPI

Article

Strain Modeling and Revealed Slope Motion Mechanisms of the Taoping Paleo-Landslide from InSAR Observations

Siyu Lai [1], Yinghui Yang [1,*], Qian Xu [2], Qiang Xu [1], Jyr-Ching Hu [3] and Shi-Jie Chen [1]

[1] State Key Laboratory of Geohazard Prevention and Geoenvironment Protection, Chengdu University of Technology, Chengdu 610059, China; 2023020379@stu.cdut.edu.cn (S.L.); xq@cdut.edu.cn (Q.X.); ccsj@cdut.edu.cn (S.-J.C.)
[2] College of Air Traffic Management, Civil Aviation Flight University of China, Deyang 618307, China; xuqian@cafuc.edu.cn
[3] Department of Geosciences, National Taiwan University, Taipei 10617, Taiwan; jchu@ntu.edu.tw
* Correspondence: yangyinghui19@cdut.edu.cn

Highlights

What are the main findings?

- A novel method based on InSAR phase gradients successfully models landslide strain fields, revealing localized deformation characteristics.
- The strain field reveals its advantage in detecting the boundaries of fast and slow deformation zones, providing more accurate information than displacement fields.

What are the implications of the main findings?

- InSAR-based strain field analysis of the Taoping paleo-landslide reveals compressive strain at the toe and tensile strain at the head scarp, offering insights into stress redistribution and sliding surface instability.
- A secondary landslide body was identified at the toe of the offset terrace, emphasizing the need for continued monitoring of strain redistribution and sliding surface evolution.

Abstract

The Taoping paleo-landslide poses a significant risk to local residents and critical infrastructure. However, traditional field surveys and deformation monitoring methods are often inadequate for capturing subtle, localized deformation characteristics—particularly at the head scarp and lateral margins—thereby limiting comprehensive assessments of slope instability. Surface strain data offer direct insights into internal stress redistribution during slope evolution and are essential for interpreting landslide mechanisms and forecasting failure. Given the current limitations in dense and wide-area strain monitoring technologies, this study proposes a novel method for modeling landslide strain fields based on Interferometric Synthetic Aperture Radar (InSAR) phase gradients. Using the phase gradient stacking approach, InSAR-derived phase gradients are transformed into strain-related parameters, enabling estimation of shear strain rates, principal strain rates, and their directional distributions. The application to the Taoping paleo-landslide reveals clear spatial patterns of compressive and tensile strain across the landslide body. Field investigations corroborate the InSAR-derived strain features through corresponding geomorphological evidence observed in both compressional and extensional zones. The proposed method enhances the understanding of landslide deformation behavior, supports evaluation of shear surface continuity and evolution, and offers a robust framework for early warning and risk mitigation in complex landslide-prone areas.

Check for updates

Academic Editor: Giuseppe Solaro

Received: 2 January 2026
Revised: 25 January 2026
Accepted: 26 January 2026
Published: 8 April 2026

Copyright: © 2026 by the authors. Licensee MDPI, Basel, Switzerland. This article is an open access article distributed under the terms and conditions of the Creative Commons Attribution (CC BY) license.

Keywords: Taoping paleo-landslide; phase gradient; strain rate modeling; InSAR deformation; sliding surface continuity

1. Introduction

The Taoping paleo-landslide, situated on the southern bank of the Zagu'nao River in Li County, Sichuan Province, China, lies within a deeply incised valley approximately 20 km south of the Longmenshan fault. This landslide is classified as a deep-seated colluvial landslide developed in an alpine to extremely high-relief mountainous environment. Historical monitoring has recorded multiple local collapses of this landslide since the 1980s. Notably, heavy rainfall triggered significant movement at the toe of the landslide in 2013, resulting in the destruction of residential houses and temporarily obstructing the Zagu'nao River. Currently, multiple tension cracks have developed in the middle and rear portions of the landslide, with deformation accelerating in recent years. These ongoing activities pose a direct threat to three villages, Provincial Highway S317, and two cross-river bridges located downslope. The rock mass in the locked segment is under-going progressive weakening, affected by both frequent intense regional rainfall and seismicity along the Longmenshan fault, including the expansion of slope fractures induced by the 2008 Wenchuan earthquake. This situation has significantly increased the probability of slope failure. Consequently, the landslide has been classified as a Priority Level 1 target for geological hazard prevention and control in Li County, requiring systematic monitoring and engineering mitigation measures.

The landslide deposit is predominantly composed of gravelly soil, which contains minor quantities of silt and clay particles. Locally developed clay-rich zones act as aquicludes. This deposit, in addition to the underlying phyllite of the Silurian Maoxian Group (characterized by significant weathering, well-developed fractures, and significant clast orientation) creates a dual-layer permeability system. This structure contributes to the characteristic long-period, low-rate sliding deformation of the landslide. The activity of the landslide exhibits pronounced seasonal variation: the slope remains stable during the dry season, while in the rainy season, precipitation rapidly infiltrates through surface cracks (e.g., those formed by seismic events and agricultural practices) and fractured bedrock zones. This infiltration triggers a marked increase in hydrostatic pressure within tension cracks located near the head scarp. Concurrently, the rock and soil mass within the slip zone experiences saturation-induced softening, which leads to a decrease in shear strength, thereby facilitating the progressive sliding of the frontal cover material along the steep scarp's free face at the toe. Therefore, the rear rock and soil mass undergoes unloading, which contributes to the formation of transverse tension cracks and down-dropped scarps. Throughout this process, downslope stresses become concentrated in regions where the potential slip surface is not yet fully continuous (i.e., locked segment), leading to the progressive failure of the locked rock mass. This may ultimately result in overall instability extending from the head scarp to the toe [1,2]. This coupled mechanism, characterized by "fracture-channeled water infiltration-slip zone softening-stress propagation", causes the progressive expansion of the landslide's surface deformation, posing a significant threat to the residents near the toe and to critical infrastructure, including roads and bridges.

Recent investigations into the Taoping paleo-landslide have mainly focused on time-series surface deformation analysis. Previous studies indicate that the rate of slope deformation ranges from approximately −120 mm/yr to 20 mm/yr, with the deformation spatially distributed in a radially decaying pattern originating from the center [3,4]. As a large-scale landslide exceeding 1.0 km in both length and width, the Taoping paleo-landslide is rep-

resentative of many deep-seated slope instabilities that rarely fail as a whole but instead exhibit pronounced internal deformation heterogeneity and localized secondary sliding driven by factors such as river erosion, rainfall, and seismic activity [5–21]. Conventional InSAR analyses, including PS-InSAR, SBAS, and SqueeSAR, mainly emphasize surface displacement or velocity fields [22–31]. At the slope scale, the mapped InSAR-derived displacement fields commonly exhibit strong spatial autocorrelation and gradual spatial variation, which makes it difficult to directly identify localized deformation anomalies or to distinguish hazard levels across different slope sectors. In nonurban or densely vegetated mountainous areas, these methods may suffer from limited coherent targets, atmospheric disturbances, phase unwrapping errors, or high computational costs, thereby constraining their ability to resolve localized deformation heterogeneity within large landslide bodies. Phase-gradient-based approaches, such as phase gradient stacking (PGS), partially alleviate these limitations by enhancing local deformation signals and suppressing long-wavelength noise [32–34]; however, they remain primarily focused on deformation detection and boundary delineation, and their capability to characterize the internal deformation structures and stress-related processes of large landslides remains limited.

In comparison to landslide deformation observations, the surface strain field offers a more direct representation of stress transfer and accumulation of the slope body. The strain field enables effective identification of stress concentrations, delineation of landslide boundaries, and detection of potential secondary landslide bodies, providing essential scientific evidence for early landslide identification and hazard assessment [35–39]. However, current methods for obtaining slope strain predominantly depend on single-borehole or single-well measurement techniques, including geological drilling and inclinometer monitoring [40–43]. Owing to their high labor and economic costs and restriction to localized measurements, these techniques hinder the acquisition of high-density strain data across extensive regions, such as entire landslide body. Consequently, analyzing stress concentration and instability risk across the entire slope becomes challenging when relying solely on a limited number of point-based strain measurements [44–48]. Therefore, developing a cost-effective method for large-area, high-density strain monitoring remains a key technical challenge in landslide hazard assessment and risk analysis.

This study presents a novel method for modeling the strain field of landslides based on InSAR observations, building upon recent developments in improved phase-gradient stacking techniques [38]. The approach enables the estimation of surface shear strain and principal strain rate distributions based on multiple directional deformation gradients and geometric parameters (aspect and slope angles), facilitating a quantitative assessment of strain concentration and hazard severity. The proposed method is applied to the Taoping paleo-landslide, and a detailed calculation process for deriving the strain rate field is presented. The derived strain rate characteristics are analyzed, and secondary sliding bodies are identified. Field investigations are conducted to validated the reliability of the strain-derived findings. This research offers valuable scientific insights for the engineering management and risk mitigation of this landslide.

2. Study Area and Data Sources

2.1. Overview of the Taoping Paleo-Landslide

The Taoping paleo-landslide is situated on the slope opposite the Taoping Qiang Village in Taoping Township, Li County, Sichuan Province, along the Zagu'nao River (Figure 1a). This landslide is located in the high to very-high mountainous regions of Northwestern Sichuan, ~20 km off the Longmenshan fault trace. This area features a typical monsoon climate in alpine regions, which is affected by complex topography and significant variations in elevation. Annual precipitation in this region ranges from

650 mm to 1000 mm, with the majority occurring between July and September, while winter precipitation remains relatively lower. The landslide exhibits a chair-shaped morphology, with higher elevations in the southwest and lower elevations in the northeast. Slope gradients vary from 27° to 53°, with the upper portion of the slope being relatively narrow and gradually widening downslope, showing a typical pattern of alternating steep and gentle slope segments. The landslide extends longitudinally for approximately 2700 m and has a transverse width of ~2000 m. At the toe of the landslide, the elevation is approximately 1480 m, while the head reaches an elevation of ~2710 m, resulting in a vertical relief of approximately 1230 m. These features classify the Taoping paleo-landslide as a large-scale landslide (Figure 1b).

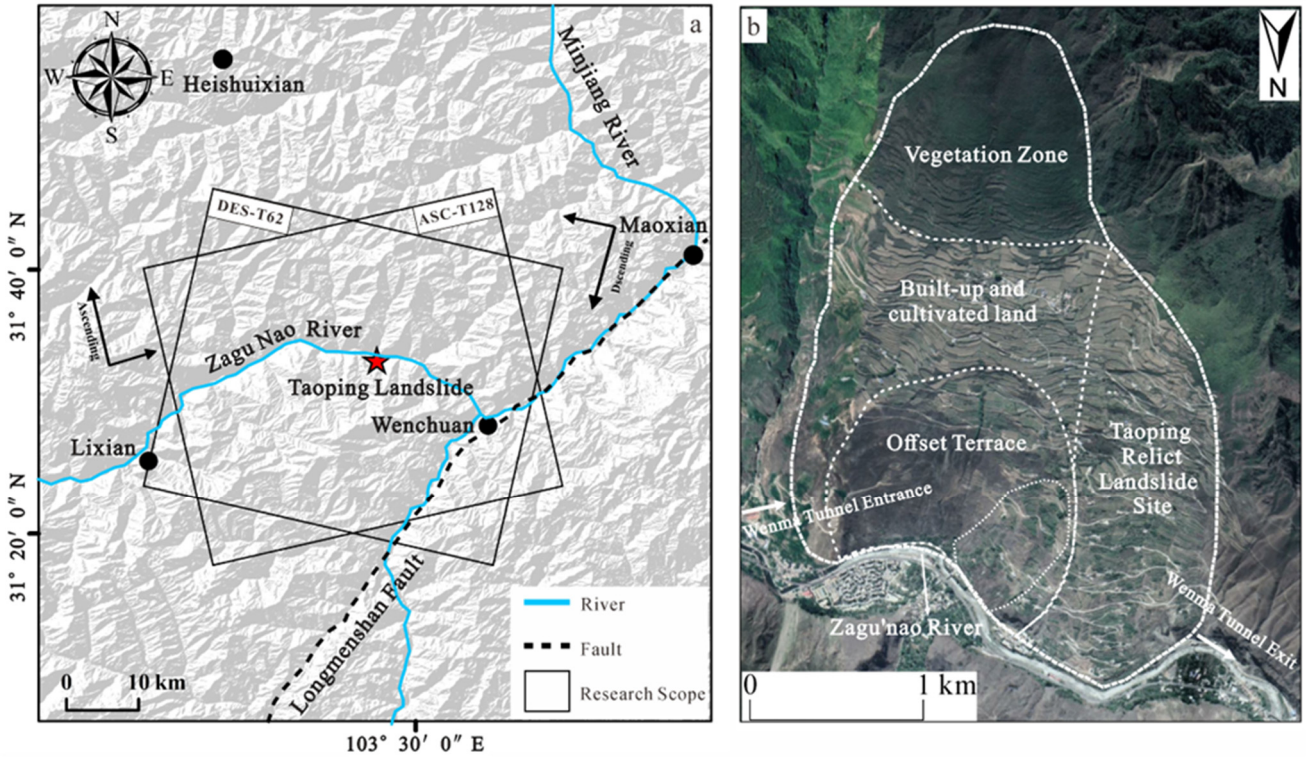


Figure 1. Overview of the study area. (**a**) Spatial coverage of the used SAR images and (**b**) optical image.

The toe of the Taoping paleo-landslide is situated along the Zagu'nao River, which originates from the Zhegu Mountain, passes through Wenchuan County, and ultimately merges with the Min River. An analysis of the topography and geo-logical characteristics reveals that the landslide can be categorized into three zones: (1) a relatively stable upper zone covered with dense vegetation; (2) a central and western zone comprising residential area, including cultivated land, roads, and buildings; and (3) an eastern offset terrace with sparse vegetation, exposed rock, and pronounced down-dropping features, where the slope exhibits inward subsidence and increased steepness. Furthermore, the deposits of the Taoping paleo-landslide are composed of gravelly silty clay and breccia-bearing silty clay, showing a high degree of looseness. Prior to the occurrence of the 2008 Wenchuan Earthquake, irrigation and drainage activities in the cultivated fields on the slope surface had already led to the development of local cracks. Following the earthquake, these cracks widened, and the slope began to undergo progressive deformation, making it highly sensitive to precipitation. The instability of the Taoping paleo-landslide presents a significant threat to the local residents' lives and property, as well as posing significant risks to critical transportation infrastructure, including the Zagu'nao River at the toe, National Highway 317, and the Wen-chuan-Maoxian Expressway.

2.2. Dataset and Processing

InSAR technology was employed to monitor the surface deformation of the landslide, which was then used to derive the associated strain fields. In this study, a series of SAR images in Interferometric Wide (IW) mode, with a spatial resolution of 5 m × 20 m, captured by Sentinel-1 satellite were collected, including 89 ascending-track and 99 descending-track acquisitions. The monitoring period extends from January 2021 to May 2024, and the detailed parameters and spatial coverage of the used SAR data can be found in Table 1 and Figure 1a, respectively. The Precise Orbit Determination (POD) data provided by the European Space Agency's (ESA) service was introduced to refine the satellite orbit vectors. The Advanced Land Observing Satellite (ALOS) World-3D Digital Elevation Model (DEM) data with a 30 m resolution was employed for modeling and the removal of the topographic phases. Furthermore, the Generic Atmosphere Correction Online Service for InSAR (GACOS) data with a spatial resolution of 90 m, were used to correct for atmospheric phase delays within the interferograms. The details of the SAR data processing are illustrated in the left panel of Figure 2. After deriving the ground deformation fields, the phase gradients and corresponding strain fields can be subsequently calculated. The detailed methodology is presented in the following Section 3, and the processing workflow is presented in the right panel of Figure 2.

Table 1. Sentinel-1A data characteristics and key SBAS-InSAR processing parameters.

Parameter Category	SAR Sensor Sentinel-1A	
Orbit direction	Ascending	Descending
Tracks	T128	T62
Incidence angle (°)	39.2	39.3
Azimuth pixel size (m)	13.9	13.9
Range pixel size (m)	2.3	2.3
Number of Images	89	99
Time span	2021.01.10~2024.05.06	2021.01.05~2024.05.25
Multi-looking factor	5 × 1	5 × 1
Temporal baseline threshold (days)	60	60
Spatial baseline threshold (m)	200	200
Phase filtering	Adaptive phase filter	Adaptive phase filter
Phase unwrapping method	Minimum Cost Flow (MCF)	Minimum Cost Flow (MCF)

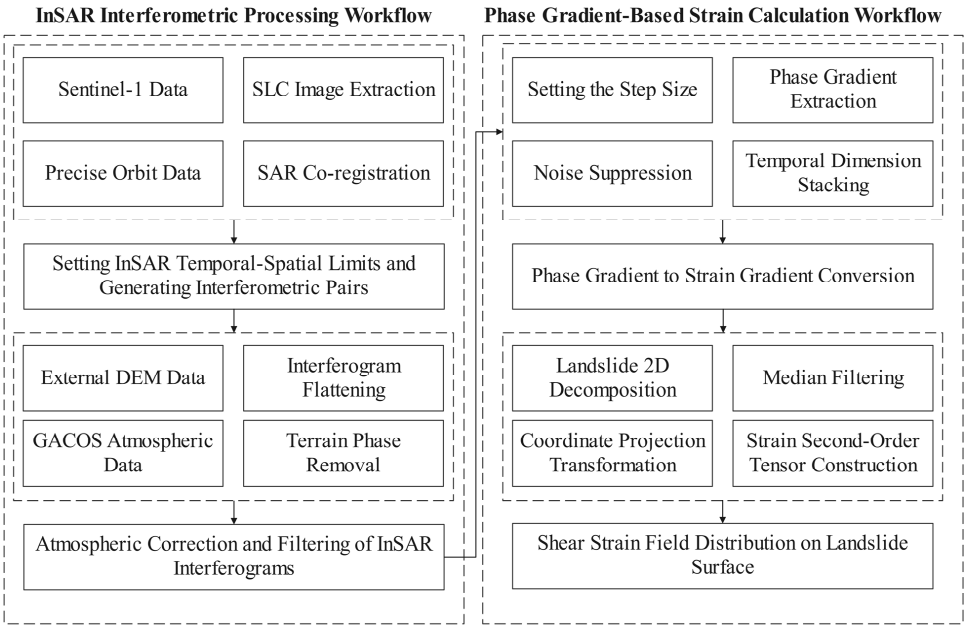


Figure 2. Technical flowchart of the SAR data processing and strain field calculation.

3. Methods

3.1. InSAR Phase Gradient Extraction

InSAR phase gradients are high sensitive to localized deformation signals [49], however noise suppression is essential. After correcting orbital errors via a quadratic fit to the interferometric phases, atmospheric delays remain the primary error in the interferogram. Atmospheric noise and ground deformation share similar low-frequency spatial correlation; however, they exhibit distinct temporal characteristics: atmospheric noise is temporal uncorrelated, whereas deformation signals are strongly related to the interferometric temporal baseline. Hence, the temporal stacking of phase gradients can effectively mitigate atmospheric noise, enhancing the clarity of local deformation signals.

For each pixel (m,n) in the i-th differential interferogram, the spatial gradients in four directions are calculated, with m and n representing the row and column indices of the pixel within the interferogram, respectively. For instance, the phase gradient in the SE direction $\Delta\varphi_i^{se}(m,n)$ is determined by incorporating a variable step size phase difference [38]. φ_i represents the phase of the i-th differential interferogram (Equation (1)), for the pixel (m,n), the phase gradient of the M differential interferograms is computed, with the pixel situated in the SE direction relative to the M phase gradient. This computation is accomplished through the stacking of phase gradients from multiple interferograms (Equation (1)), which effectively mitigates noise, including atmospheric interference, and produces the corresponding phase gradient data $\Delta\varphi^{se}$.

$$\Delta\varphi^{se}(m,n) = \sum_i^M \{\varphi_i(m+s,n+s) - \varphi_i(m-s,n-s)\} \quad (1)$$

where s denotes the spatial step size (in pixels) used to compute the phase difference between two pixels symmetrically located around pixel (m, n). When s = 1, the phase gradient is calculated between immediately adjacent pixels, providing the highest sensitivity to localized deformation but also being more susceptible to noise. Larger values of s correspond to phase differences computed over a broader spatial interval, which effectively enhances spatial smoothing and noise suppression at the expense of reduced sensitivity to small-scale deformation features. In this study, the parameter s is selected to balance local deformation resolution and noise robustness in the phase gradient estimation.

According to the procedure delineated above, the phase gradient data for the remaining three directions (eastward $\Delta\varphi^{e}$, northward $\Delta\varphi^{n}$, and northeastward $\Delta\varphi^{ne}$) can be acquired. Subsequently, these phase gradient data are amalgamated (Equation (2)) to derive the integrated phase gradient data for the slope.

$$\varphi = \sqrt{\frac{(\Delta\varphi^{se})^2 + (\Delta\varphi^{ne})^2 + (\Delta\varphi^{n})^2 + (\Delta\varphi^{e})^2}{4}} \quad (2)$$

3.2. Strain Field Calculation via Phase Gradients

Multidirectional phase gradients serve as indicators of the deformation characteristics associated with landslides. However, strain is a more direct and physically significant metric. Strain effectively characterizes the variation in deformation across different directions, particularly in regions experiencing localized stretching, compression, and shearing, which are essential for a comprehensive analysis of landslide zones. Consequently, this study employs phase gradients derived from differential interferograms across multiple directions to inform spatial numerical analyses, thereby constructing the strain field for each direction. Specifically, the relationship between the phase gradient in a single direction $\Delta\varphi$ and the strain ε is articulated in Equation (3).

$$\varepsilon = -\frac{\Delta\varphi}{4\pi} \times \frac{\lambda}{L} \times 10^6 \tag{3}$$

where L is the scale factor defined by the satellite's resolution, λ is the radar wavelength, 10^6 is the unit conversion factor.

Furthermore, the ascending and descending track LOS phase gradient could be decomposed into lateral and vertical strain components that are aligned with the slope direction [3,50–53]. And the calculation model is expressed as follows:

$$\begin{bmatrix} a_{asc} & b_{asc} \\ a_{des} & b_{des} \end{bmatrix} \begin{bmatrix} dV_{DK}/dx \\ dV_{DT}/dx \end{bmatrix} = \begin{bmatrix} dV_{asc}/dx \\ dV_{des}/dx \end{bmatrix} \tag{4}$$

where

$$\begin{cases} a = -\cos\theta\sin\alpha + \sin\theta\sin\varphi\cos\alpha\cos\beta \\ -\sin\theta\cos\varphi\cos\alpha\sin\beta \\ b = \sin\theta\sin\varphi\sin\beta + \sin\theta\cos\varphi\cos\beta \end{cases} \tag{5}$$

where a and b represent the projection parameters of horizontal and vertical strain to the strain along the LOS direction. It should be noted that these parameters are not only due to the satellite incidence angle θ and the flight direction φ, but also associate to the characteristics of the landslide, including the slope angle α and the aspect direction of the slide β. x corresponds to the projection directions, such as EW, NS, NE, or SE. dV_{asc}/dx and dV_{des}/dx represent the LOS phase gradients in the projection direction. dV_{DK}/dx and dV_{DT}/dx represent the horizontal and vertical strain components in the projection axes, respectively.

Based on the aforementioned process, the strain gradients in both the slope direction and the vertical direction can be determined based on the gradients measured in each respective direction (e.g., NS, EW, NE, and SE) in Figure 3. Finally, the relevant gradient components are modeled by Equation (6), allowing for the computation of strain components both along the slope and perpendicular to the slope.

$$\begin{cases} \varepsilon_{DK} = \dfrac{\dfrac{dV_{DK}}{dx}\sin\beta + \dfrac{dV_{DK}}{dy}\cos\beta}{\cos\alpha} + \dfrac{\dfrac{dV_{DK}}{dy_1}\sin\left(\theta_{diag}-\beta\right) - \dfrac{dV_{DK}}{dx_1}\cos\left(\theta_{diag}-\beta\right)}{\cos\alpha} \\ \varepsilon_{DT} = \dfrac{dV_{DK}}{dy}\sin\beta - \dfrac{dV_{DT}}{dx}\cos\beta - \dfrac{dV_{DT}}{dx_1}\cos\left(\theta_{diag}-\beta\right) - \dfrac{dV_{DT}}{dy_1}\sin\left(\theta_{diag}-\beta\right) \end{cases} \tag{6}$$

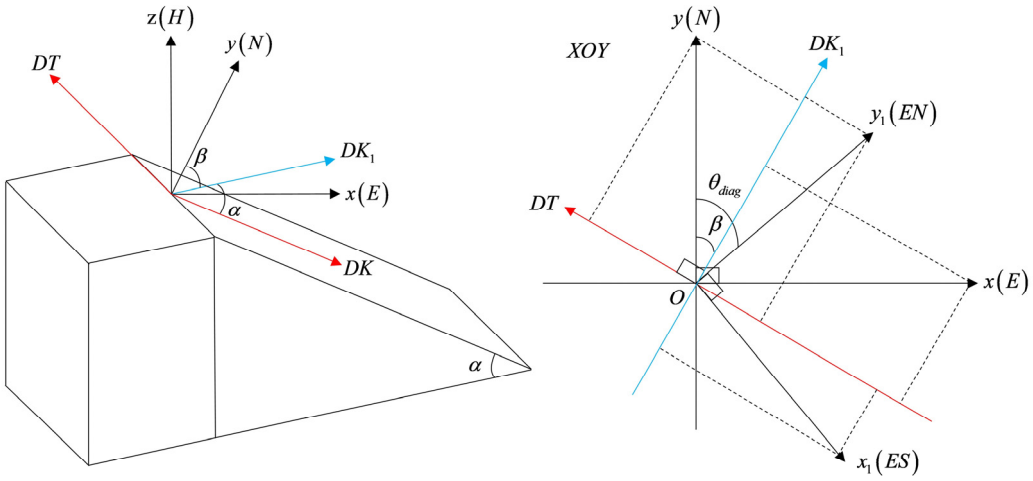


Figure 3. Projection relationship of the slope surface coordinate system and geographic coordinate system (XOY Plane: Plan View).

For the landslide plane, the two strain components in Equation (6) not only characterize the stretching or compressive properties of surface deformation in both the slope direction and the vertical direction, but also form the second-order symmetric strain tensor. To further quantify the overall intensity of shear deformation on the landslide plane, shear strain is calculated [54], in addition to the maximum and minimum principal strains. These principal strains elucidate the directional characteristics of surface deformation and provide insights into the stress distribution patterns associated with the landslide. The shear strain ε_{shr} is expressed as follows:

$$\varepsilon_{shr} = \sqrt{(\varepsilon_{xy})^2 + \frac{1}{4}(\varepsilon_{xx} - \varepsilon_{yy})^2} \quad (7)$$

where ε_{xy} represents the shear strain component in the second-order strain tensor, while ε_{xx} and ε_{yy} represent the strain components along the slope direction and vertical slope direction, respectively. Which can be calculated based on Equation (6).

4. Ground Velocity and Strain Fields of the Taoping Paleo-Landslide

4.1. Velocity Field of the Taoping Paleo-Landslide

Figure 4 depicts the average line-of-sight (LOS) velocity maps from ascending and descending tracks using the SBAS-InSAR technology [53]. It can be observed that the ground deformation rates of the two InSAR tracks differ in both the magnitude and spatial distribution. The ascending-track velocities range from –120 mm/yr to 20 mm/yr, yielding a maximum difference of 140 mm/yr. In comparison, the deformation rate for the descending track ranges from –80 mm/yr to 20 mm/yr, with a maximum variation of 100 mm/yr. These variations may be attributed to several factors: Firstly, the side-looking imaging geometries of the ascending and descending tracks are distinct. Secondly, the Taoping paleo-landslide area is characterized by significant topographic relief, which can lead to geometric distortion in SAR imagery, thereby affecting the accuracy of the observed data. Thirdly, the differing observation times of the ascending and descending track images contribute to variations in atmospheric noise components, which further affect the accuracy of the deformation observations [55,56].

Both ascending- and descending-track InSAR observations indicate that significant deformation rates are concentrated in the offset terrace, exhibiting a radial decrease from the center. However, both InSAR tracks suffer from a lack of reliable data in the densely vegetated regions due to interferometric decorrelation. This limitation arises from the inability of the C-band radar utilized by the Sentinel-1 satellite to penetrate the dense vegetation cover in these areas. Furthermore, the descending InSAR field exhibits both positive and negative signals at the toe of the landslide, indicating the complexity of deformation in this area. This suggests that different zones within the slope toe may be undergoing varied movement patterns. However, the inherent ambiguity of the InSAR observations prevents a definitive determination of whether this phenomenon results from secondary landslide activity or localized acceleration of deformation. This issue will be further analyzed in the subsequent section addressing the strain fields.

4.2. Phase Gradient Extraction

The phase gradients in the NS, EW, NE, and SE directions are derived first based on Equation (1). Building upon these directional gradients, the integrated phase gradients are then computed using Equation (2). However, the significant differences in magnitude among the directional gradients present challenges for direct integration, as they may introduce directional bias and reduce the reliability of the composite result. To address this issue, a normalization process is applied to rescale the multi-directional gradients

values to a standardized, dimensionless range of 0 to 1. It helps mitigate the effects of scale disparities among directions and balances the contributions of multi-directional gradients. The derived integrated phase gradients are presented in Figure 5.

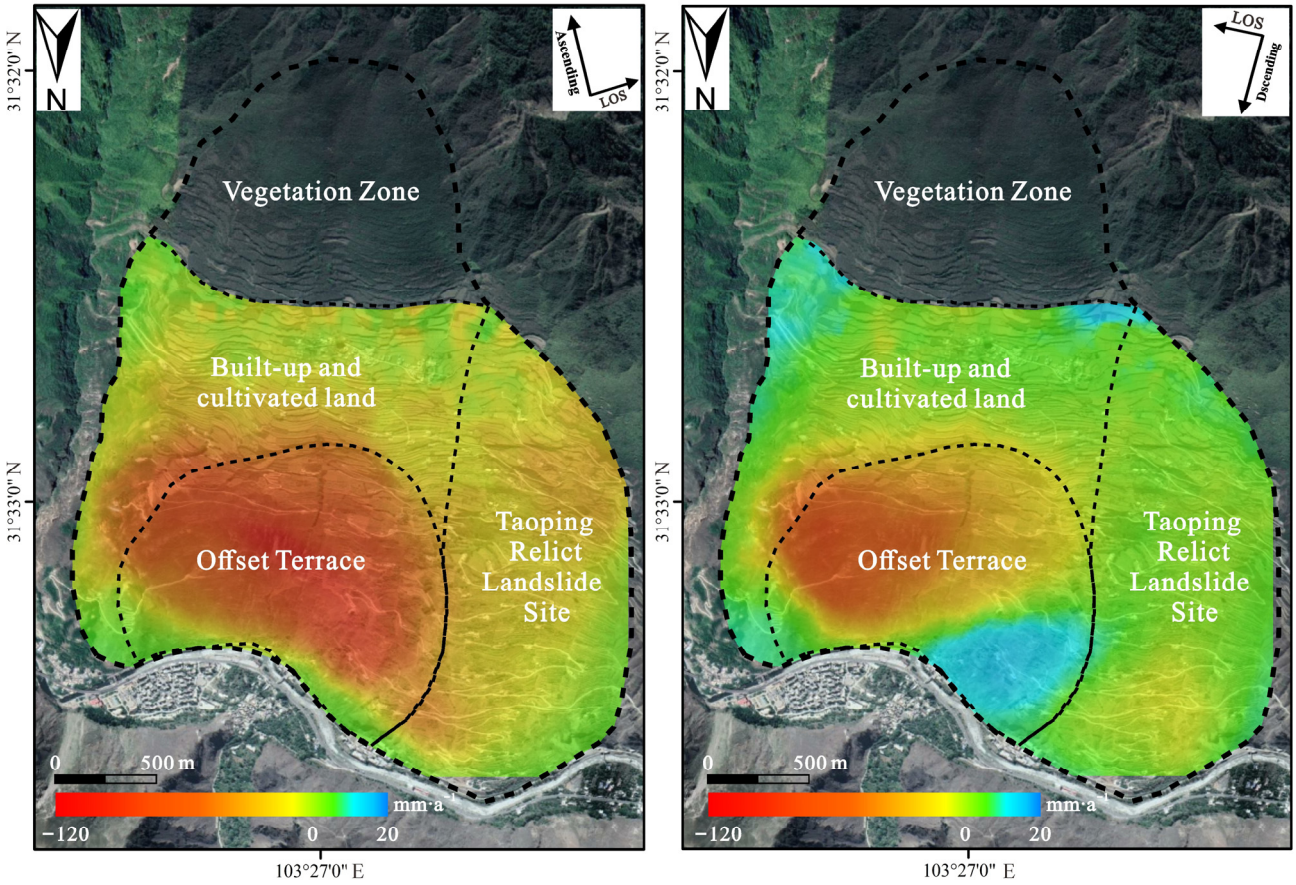


Figure 4. Velocity fields of the Taoping paleo-landslide from ascending (**left**) and descending (**right**) InSAR tracks. The blue colors represent a decrease in slant range, indicating surface movement toward the satellite, whereas red colors indicates an increase, corresponding to movement away from the satellite.

The gradient data derived from the ascending track indicate a localized concentration of high-gradient values (greater than 0.8) at the toe of the landslide, spatially corresponding to the compression zone identified in the subsequent shear strain rate field. In contrast, the descending track not only captures gradient anomalies at the landslide toe but also reveals additional anomalies along the slope's sidewall and rear tensile zone, with a peak value of 0.55. These findings highlight the complementary advantages of multi-track InSAR observations for characterizing complex slope deformation, particularly in areas with heterogeneous terrain conditions.

While phase gradients can effectively recognize the overall deformation concentration within a landslide, they are limited in identifying localized high-risk areas. This limitation arises from the fact that landslide deformation predominantly occurs along the slope and slope-perpendicular directions [3,4], whereas the InSAR technique maps the deformation along the LOS direction. Topographic variations affect the SAR imaging geometry, leading to distortions such as shadowing and layover, which further reduce the ability of the phase gradient field to accurately delineate deformation boundaries and the spatial distribution of secondary sliding zones. Furthermore, calculating the strain components along both the slope and slope-perpendicular directions, as well as the shear strain on the slope surface, may effectively mitigate this limitation.

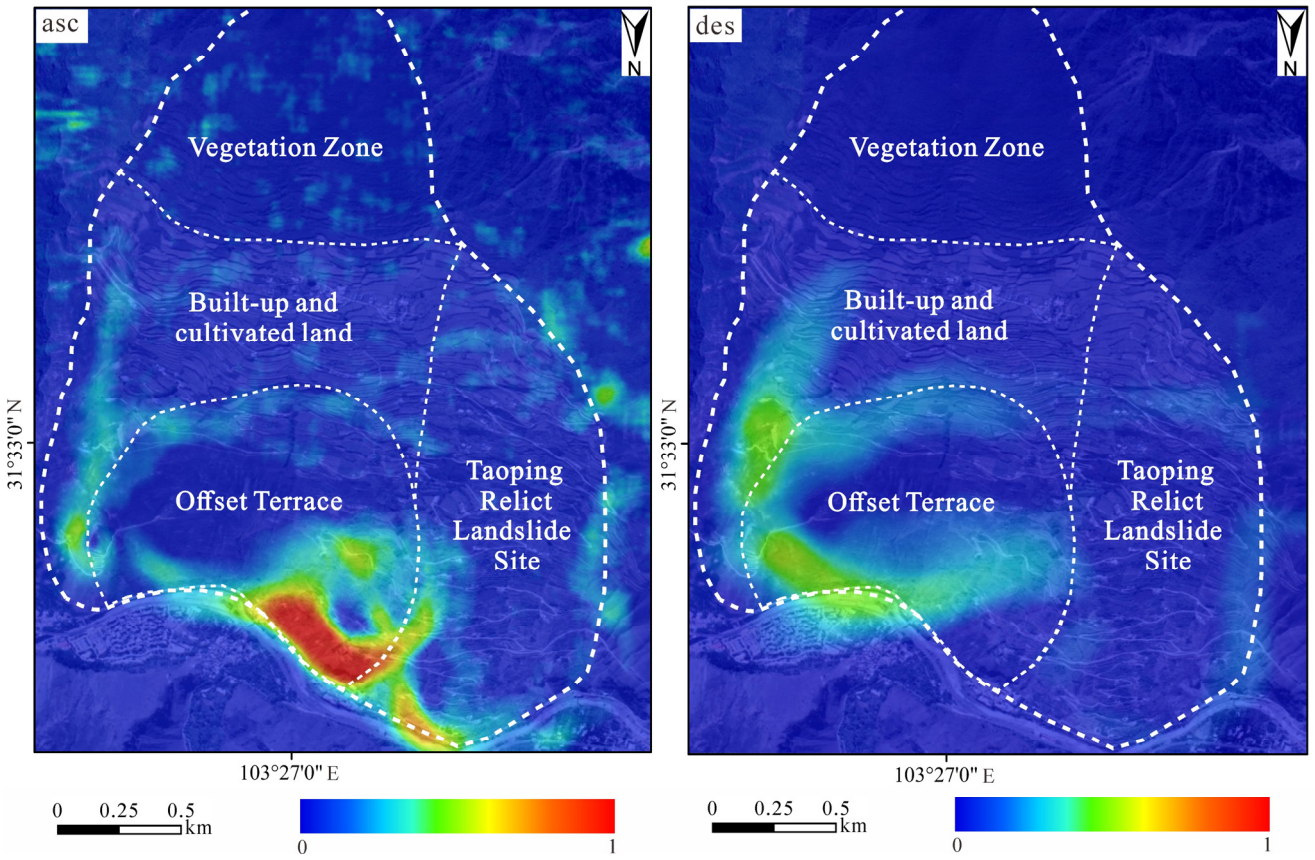


Figure 5. Derived phase gradient maps from the ascending- and descending-track InSAR velocity fields.

4.3. Taoping Paleo-Landslide Strain Field Modeling

The gradient data in four directions, derived from the ascending- and descending-track observations, were jointly utilized to calculate the strain rate fields along the slope and slope-perpendicular directions, based on the method described in Section 3.2. The derived strain rate fields are shown in Figure 6. In the strain rate field along the slope (Figure 6a), a pronounced high-strain-rate belt, with a peak value of approximately 2500 με/yr, is observed at the toe of the landslide. Its spatial distribution suggests a correlation between the strain concentration and the terrain morphology. Furthermore, an anomalous zone with negative strain rates of approximately –1500 με/yr, is observed along the left sidewall and in the head region of the landslide, suggesting the potential presence of tensile components in this area. The alternating distribution of positive and negative strain further highlights the spatial heterogeneity of deformation within the slope body.

The slope-perpendicular strain rate field (Figure 6b) reveals negative strain rates along both lateral boundaries of the slope, with peak values reaching –500 με/yr, while the central region predominantly exhibits positive strain anomalies of up to 500 με/yr. This pattern results in a saddle-shaped strain distribution, indicative of lateral confinement effects acting on the landslide body. The regions of high strain rate in both the slope-parallel and slope-perpendicular strain rate fields are not spatially continuous; instead, they manifest as discrete local anomalies. This phenomenon may be attributed to variations in the thickness of local cover layers, heterogeneity in the geotechnical structure, and differences in surface hydrology [57,58].

To investigate the characteristics of the strain field associated with the Taoping paleo-landslide, the shear strain magnitude, along with the maximum and minimum principal strain rates, was calculated based on the strain components in both the slope-parallel

and slope-perpendicular directions (Figure 7). The strain rate field of the Taoping paleo-landslide exhibits pronounced spatial heterogeneity, characterized by an east–west zonation and a north–south segmentation pattern. On the eastern flank, a high shear strain zone extends approximately EW at the toe of the Taoping relict landslide site, forming a compressive front edge zone about 400 m wide. In this area, the direction of principal strain is nearly aligned with the slope direction, with the peak strain rate reaching up to 700 με/yr. Concurrently, a localized zone with appreciable tensile strain rate (~300 με/yr) is observed at the upper section of the right sidewall of Taoping relict landslide site, indicating that the geotechnical material of the sidewall is experiencing a progressive tensile cracking process, which results in localized tensile stress concentration. However, no distinct zone of tensile strain rate concentration has developed in the head area of the relict landslide site. This suggests that a newly formed tensile fracture plane with a clear spatial orientation has not yet emerged, indicating a low probability of overall slope failure.

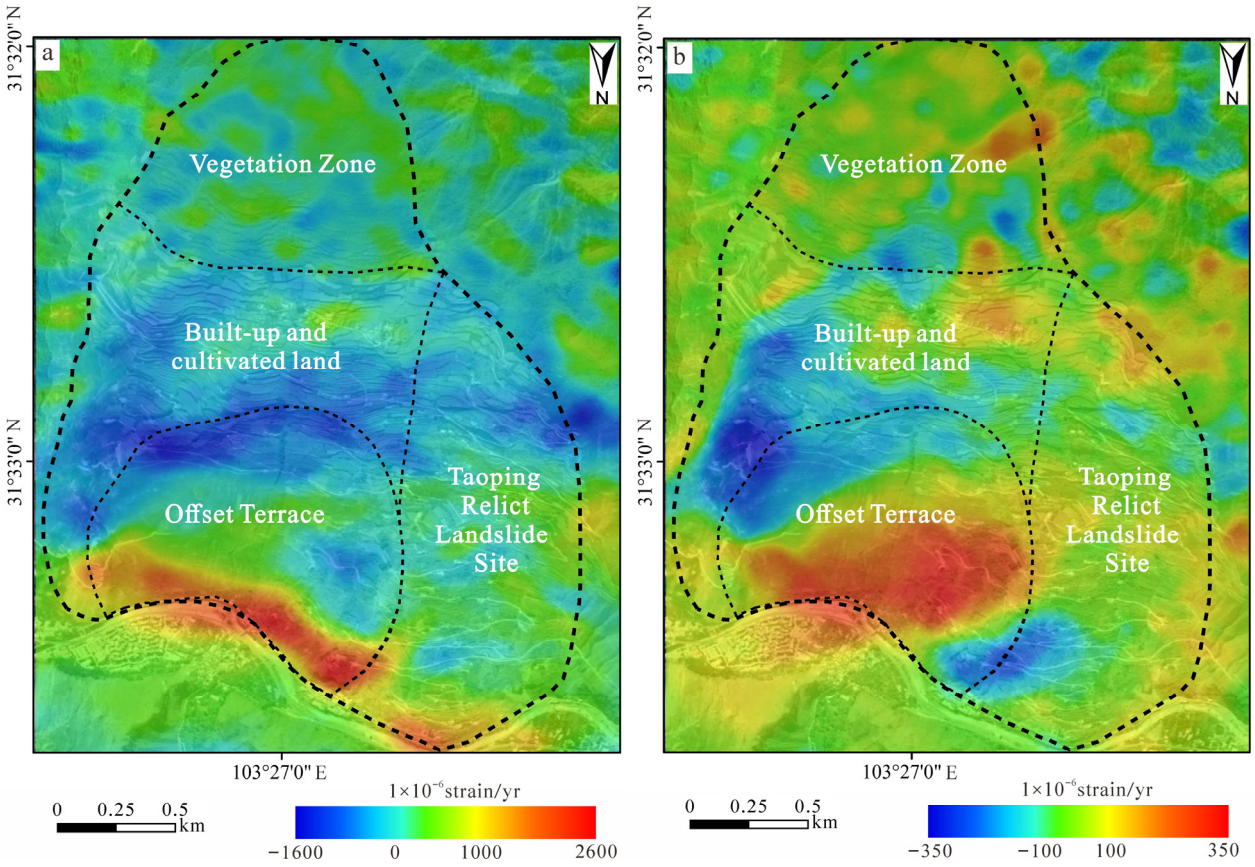


Figure 6. Strain rates along the slope (**a**) and slope-perpendicular (**b**) directions.

In contrast, the strain distribution pattern observed in the offset terrace on the eastern side of the paleo-landslide (left side of Figure 7) is more complex. The shear strain field exhibits greater shear strain in the northern region and weaker shear strain in the south. A pronounced shear strain rate concentration extends NW-SE at the toe of the offset terrace, spanning approximately 1.2 km with a peak strain rate of 1200 με/yr. The direction of principal strain is nearly aligned with the slope orientation, underscoring the role of the compressive locking zone at the toe in regulating stress transmission. Additionally, distinct zones of concentrated tensile strain rates have been identified in the head area and the upper left sidewall of the offset terrace, with peak values reaching approximately 900 με/yr. No continuous tensile strain rate anomaly zone is observed along the lower left sidewall and the right sidewall, suggesting that the developing sliding surface within the offset

terrace has not yet achieved full connectivity. Nevertheless, this area presents significant potential risks and necessitates ongoing monitoring.

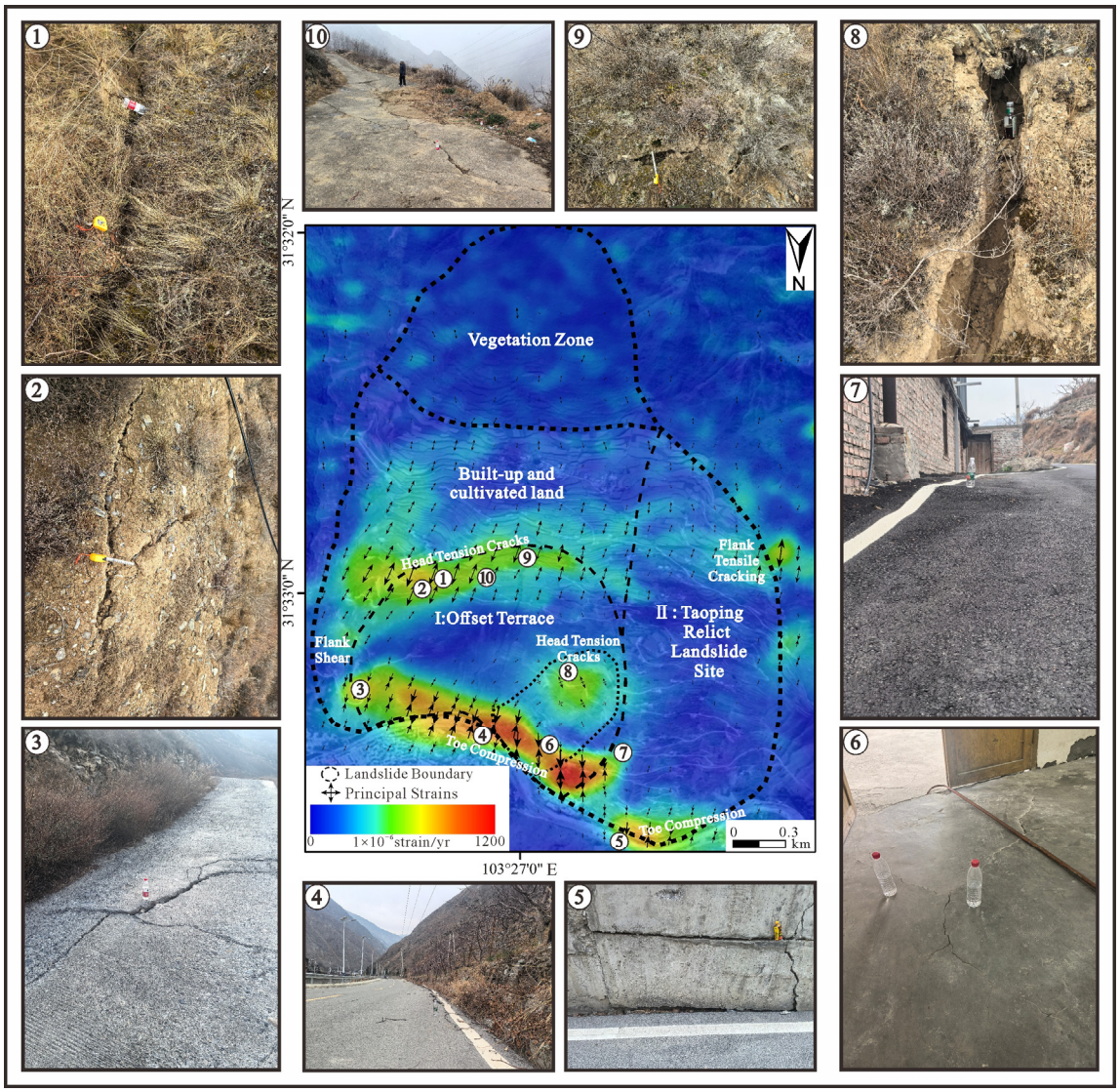


Figure 7. Shear strain rate distribution of the Taoping paleo-landslide and field investigation. Regions I and II denote landslide offset terrace and paleo-landslide relics, respectively. Cross arrows indicate principal strain magnitude/direction, opposing arrowheads represent compression while tails facing each other indicate tension. Field sites 1 to 10 are indicated by circle markers.

In the vicinity of the toe on the right side of the offset terrace, the principal strain vectors exhibit a clockwise deflection ranging from 16° to 24°, as supported by the presence of a tensile crack near site 8 in the head scarp region (Figure 7). Combined with the localized anomalies in the tensile strain rate observed in the upper region, it can be inferred that this area is undergoing a phase of strain reorganization. The bulging of the retaining wall at site 5 near the toe, together with the development of compressive fissures (Figure 7), further supports the inference that this area is evolving into a secondary sliding unit with an independent displacement direction, indicating the potential onset of a secondary landslide.

5. Discussion and Analysis

To assess the reliability of the landslide strain rate distribution derived from InSAR phase gradients, a field survey and comparative analysis were conducted. The field survey

revealed significant tensile cracking at the rear edge of the offset terrace and the secondary landslide body. Several surface cracks observed at sites 1 and 2 (Figure 7), aligned with the direction of the tensile strain rate vectors. This observation corroborates the tensile mechanism at the rear edge and demonstrates that the InSAR-derived strain field effectively captures the tensile strain in this area. Conversely, in the compressive region at the front edge indicated by the strain rate field, the field survey revealed different local geotechnical compression features, including bulging along the edges of surface roads and uplift of floors in local residences (sites 4–6 in Figure 7). Specifically, in proximity to the front edge locking zone, the surface material exhibited increased thickness, and compression traces were discernible (site 4 in Figure 7), consistent with the high compression features depicted in the strain rate field. This further substantiates that the landslide front serves as a stress concentration zone, reflecting the intense deformation and material accumulation at the forefront of the Taoping paleo-landslide.

In the region adjacent to the landslide sidewall, field survey results align well with strain analysis. Localized shear failure and tensile cracks were observed at the field site 3 (Figure 7), located on the left sidewall of landslide, where a localized shear strain rate anomaly is present. It suggests that the area exhibits relatively poor stability and has experienced both tensile cracking and shear failure. In contrast, no significant tensile or shear failures were found on the right sidewall of the landslide, suggesting that this area maintains a relatively higher overall stability, consistent with the lower strain rate values indicated by the InSAR-derived strain fields. Furthermore, visible ground fissures were identified at site 8 (Figure 7) within the rear tensile strain anomaly zone at the head of the secondary landslide body. This indicates that this region is undergoing active deformation, with the sliding surface potentially propagating from the rear scarp toward the toe of the slope. Additionally, given the pronounced compressive features observed at the landslide toe (sites 6 and 7 in Figure 7) and the ongoing fluvial erosion by the Zagu'Nao River, the potential hazard posed by this secondary slope is considerable, warranting sustained high-resolution monitoring.

The field investigation did not identify any significant tensile cracks above the offset terrace or at the rear edge of the relict landslide site. This suggests that the slope stabilization measures have effectively mitigating the downward movement of the local slope, particularly at the front edge area where intense compressive deformation remains limited. However, the ongoing downward movement of material—particularly at the rear edge of the offset terrace and newly formed secondary landslide's rear edge—will continue to exert pressure on the front edge region of the slope. This may promote the development and connectivity of the sliding surfaces. Therefore, continuous monitoring of the strain accommodation along the sidewalls and front edge of the slope is imperative, with particular attention to the potential connectivity of the sliding surfaces at the rear edge, sidewalls, and front edge.

It should be noted that this research focuses on surface strain field extraction based on InSAR data. Given the inherent limitations of radar remote sensing, the current analysis captures only strain at or near the surface, without direct insight into subsurface deformation, which may be more complex. A more complete understanding of the landslide's three-dimensional strain behavior should, in the future, involve geophysical surveys, borehole-based monitoring, and in situ strain measurement methods. This integration is essential for accurate assessments of deep-seated landslide mechanisms and effective hazard mitigation.

6. Conclusions

In this study, the deformation characteristics and strain rate distribution of the Taoping paleo-landslide are comprehensively investigated. A novel method for landslide strain modeling based on InSAR phase gradients is proposed. By integrating InSAR measurements with field investigation data, the spatial patterns of landslide deformation and strain rate distribution are analyzed, revealing the internal stress transfer mechanisms and potential instability zones within the slope. The primary conclusions are outlined as follows: (1) Time-series InSAR data not only enable accurate extraction of surface deformation but also facilitate reliable modeling of landslide strain fields. (2) The derived strain rate field effectively captures the spatial distribution of tensile and compressive deformation zones, particularly highlighting strain anomalies at the rear edge and sidewalls, thereby providing quantitative evidence for evaluating sliding surface connectivity and instability risk. (3) The offset terrace within the Taoping paleo-landslide remains a critical area of concern, where a newly developing secondary landslide body has been identified at the toe, necessitating continued monitoring of strain redistribution and sliding surface evolution.

The application of the proposed strain modeling method to the Taoping paleo-landslide demonstrates its practical effectiveness for landslide deformation analysis and risk assessment. The InSAR-derived strain rate fields show good consistency with geomorphological features and deformation phenomena observed during field investigations, such as tensile cracking at the rear edge and compressive deformation at the landslide toe. Compared with conventional displacement-based InSAR analyses, the strain-based approach provides additional insight into deformation heterogeneity and sliding surface continuity, thereby improving the interpretability of landslide deformation processes in the Taoping landslide area.

It should be emphasized that the proposed strain modeling approach is based on surface deformation derived from InSAR observations and does not directly measure subsurface deformation or internal stress conditions. The interpretation of surface strain as an indicator of internal stress redistribution is therefore indirect and subject to the assumption that surface deformation gradients reasonably reflect underlying deformation processes. In addition, the model is developed under the assumption of negligible normal deformation along the sliding surface, consistent with the parallel displacement hypothesis commonly adopted for translational landslides. While these assumptions are appropriate for landslides dominated by downslope sliding with relatively simple deformation patterns, their applicability to rotational landslides or landslides with complex deep-seated deformation mechanisms may be limited. For such cases, integration with subsurface monitoring techniques and further model development would be required.

Author Contributions: Conceptualization: S.L., Y.Y., Q.X. (Qiang Xu) and J.-C.H.; Methodology: S.L. and Y.Y.; Software: S.L.; Validation: S.L. and Q.X. (Qian Xu); Resources: Q.X. (Qiang Xu); Data curation: S.L.; Writing—Original draft preparation: S.L.; Writing—Review and editing: S.L., Y.Y. and Q.X. (Qian Xu); Visualization: S.L.; Supervision: Y.Y., Q.X. (Qian Xu) and Q.X. (Qiang Xu); Funding acquisition: Y.Y.; Field investigation: S.L., S.-J.C. and Q.X. (Qian Xu). All authors have read and agreed to the published version of the manuscript.

Funding: This research is supported by the National Natural Science Foundation of China (Grant No. 42474041 and 42471485), Sichuan Provincial Merit-Based Program for Returned Overseas Scholars' Scientific & Technological Activities (No. 10900-25BZ27-01-2025), Sichuan Province Philosophy and Social Science Planning Major Project, China (SCJJ23WT06), State Key Laboratory of Geohazard Prevention and Geoenvironment Protection Independent Research Project (SKLGP2021Z016).

Data Availability Statement: 1. Data Availability: The Sentinel-1 imagery used in this study was obtained from the Alaska Satellite Facility (ASF) https://search.asf.alaska.edu, accessed on 31 January

2026. The data can be accessed and downloaded directly from the ASF portal under the appropriate project identifier. 2. Software Availability: The code used for processing the data is openly available on GitHub. It can be accessed and downloaded via the following link: https://github.com/DAYU0607/my-landsat-code.git, accessed on 31 January 2026. Data visualization was performed using Generic Mapping Tools (GMT), a free tool for creating high-quality maps and visualizing geospatial data, available at https://www.generic-mapping-tools.org/, accessed on 31 January 2026. And all the figures are mapped based on the Generic Mapping Tools (GMT, v6.4.0) software.

Conflicts of Interest: The authors acknowledge that there are no conflicts of interest.

References

1. Chen, L.; Chen, J. Characteristics analysis and stability study of the Taoping landslide in Taoping Township, Lixian County. *Sci. Technol. Enterp.* **2011**, *15*, 134–135, 137. [CrossRef]
2. Wang, D.S.; Liu, H. Characteristics analysis and stability study of the Taoping landslide in Taoping Township, Lixian County. *Technol. Commun.* **2011**, *4*, 119.
3. Shi, G.L.; Chen, H.; Liu, X.W.; Yang, Y.H.; Xu, X.; Zhao, J.J. Deformation velocity field along aspect directions of an ancient landslide at Taoping village derived from ascending and descending Sentinel-1A data. *J. Eng. Geol.* **2022**, *30*, 1350–1361.
4. Yang, C.; Yang, Y.H.; Wang, J.Y.; Xu, Q.; Chen, Q.; Tao, X.X.; Hu, Z.Q. Inferring landslide depth based on ascending and descending InSAR deformation—Example of Taoping village ancient landslide. *J. Eng. Geol.* **2023**, *31*, 868–879. [CrossRef]
5. Terzaghi, K.; Paige, S. Mechanism of landslides. In *Application of Geology to Engineering Practice*; Geological Society of America, Inc.: New York, NY, USA, 1950; pp. 83–123. [CrossRef]
6. Goldstein, R.M.; Engelhardt, H.; Kamb, B.; Frohlich, R.M. Satellite radar interferometry for monitoring ice sheet motion: Application to an Antarctic ice stream. *Science* **1993**, *262*, 1525–1530. [CrossRef] [PubMed]
7. Huang, R.Q. Large-scale landslides and their sliding mechanisms in China since the 20th century. *Chin. J. Rock. Mech. Eng.* **2007**, *26*, 433–454.
8. Dai, F.C.; Lee, C.F.; Ngai, Y.Y. Landslide risk assessment and management: An overview. *Eng. Geol.* **2002**, *64*, 65–87. [CrossRef]
9. Rotaru, A.; Oajdea, D.; Răileanu, P. Analysis of the landslide movements. *Int. J. Geol.* **2007**, *1*, 70–79.
10. Liu, C.Z. Epistemology and methodology on geo-hazard research. *J. Eng. Geol.* **2015**, *23*, 809–820. [CrossRef]
11. Liu, C.Z. Analysis methods on the risk identification of landslide disasters. *J. Eng. Geol.* **2019**, *27*, 88–97. [CrossRef]
12. Liu, C.Z.; Chen, C.L. Achievements and countermeasures in risk reduction of geological disasters in China. *J. Eng. Geol.* **2020**, *28*, 375–383. [CrossRef]
13. Cao, Y. Risk Assessment and Early Warning of Individual Landslide—Case Study of the Tangjiao Landslide in Wanzhou. Master's Thesis, China University of Geosciences, Beijing, China, 2016.
14. Dong, J.; Zhang, L.; Tang, M.; Liao, M.; Xu, Q.; Gong, J.; Ao, M. Mapping landslide surface displacements with time series SAR interferometry by combining persistent and distributed scatterers: A case study of Jiaju landslide in Danba, China. *Remote Sens. Environ.* **2018**, *205*, 180–198. [CrossRef]
15. Froude, M.J.; Petley, D.N. Global fatal landslide occurrence from 2004 to 2016. *Nat. Hazards Earth Syst. Sci.* **2018**, *18*, 2161–2181. [CrossRef]
16. Lin, Q.; Wang, Y. Spatial and temporal analysis of a fatal landslide inventory in China from 1950 to 2016. *Landslides* **2018**, *15*, 2357–2372. [CrossRef]
17. Feng, W.; Dun, J.; Yi, X.; Zhang, G. Deformation analysis of Woda Village old landslide in Jinsha River Basin using SBAS-InSAR technology. *J. Eng. Geol.* **2020**, *28*, 384–393. [CrossRef]
18. Wang, Y.; Dong, J.; Zhang, L.; Deng, S.; Zhang, G.; Liao, M.; Gong, J. Automatic detection and update of landslide inventory before and after impoundments at the Lianghekou reservoir using Sentinel-1 InSAR. *Int. J. Appl. Earth Obs. Geoinf.* **2023**, *118*, 103224. [CrossRef]
19. Liu, Z.J.; Qiu, H.J.; Zhu, Y.R.; Huangfu, W.C.; Ye, B.F.; Wei, Y.D.; Tang, B.Z.; Kamp, U. Increasing irrigation-triggered landslide activity caused by intensive farming in deserts on three continents. *Int. J. Appl. Earth Obs. Geoinf.* **2024**, *134*, 104242. [CrossRef]
20. Jiang, K.; Yang, Y.H.; Xu, Q.; Li, L.; Li, P.F.; Li, H.L.; Chen, Q. Friction residual estimation and landslide risk assessment based on InSAR deformation. *J. Eng. Geol.* **2024**, *32*, 889–903. [CrossRef]
21. Qiu, H.J.; Li, Y.J.; Zhu, Y.R.; Ye, B.F.; Yang, D.D.; Liu, Y.; Wei, Y.D. Do post-failure landslides become stable? *Catena* **2025**, *249*, 108699. [CrossRef]
22. Zebker, H.A.; Villasenor, J. Decorrelation in interferometric radar echoes. *IEEE Trans. Geosci. Remote Sens.* **1992**, *30*, 950–959. [CrossRef]
23. Zebker, H.A.; Rosen, P.A.; Goldstein, R.M.; Gabriel, A.; Werner, C.L. On the derivation of coseismic displacement fields using differential radar interferometry: The Landers earthquake. *J. Geophys. Res. Solid Earth* **1994**, *99*, 19617–19634. [CrossRef]

24. Zebker, H.A.; Rosen, P.A.; Hensley, S. Atmospheric effects in interferometric synthetic aperture radar surface deformation and topographic maps. *J. Geophys. Res. Solid Earth* **1997**, *102*, 7547–7563. [CrossRef]
25. Ferretti, A.; Prati, C.; Rocca, F. Permanent scatterers in SAR interferometry. *IEEE Trans. Geosci. Remote Sens.* **2001**, *39*, 8–20. [CrossRef]
26. Ferretti, A.; Fumagalli, A.; Novali, F.; Prati, C.; Rocca, F.; Rucci, A. A new algorithm for processing interferometric data-stacks: SqueeSAR. *IEEE Trans. Geosci. Remote Sens.* **2011**, *49*, 3460–3470. [CrossRef]
27. Ferretti, A.; Monti-Guarnieri, A.; Prati, C.; Rocca, F.; Massonnet, D. *InSAR Principles: Guidelines for SAR Interferometry Processing and Interpretation*; ESA: Noordwijk, The Netherlands, 2007.
28. Wasowski, J.; Bovenga, F. Investigating landslides and unstable slopes with satellite multi-temporal interferometry: Current issues and future perspectives. *Eng. Geol.* **2014**, *174*, 103–138. [CrossRef]
29. Liu, G.X.; Zhang, R.; Li, T.; Yu, B.; Li, Y.F.; Zuo, H.R.; Luo, Y.J. Extracting 3D ground deformation velocity field by multi-platform persistent scatterer SAR interferometry. *Chin. J. Geophys.* **2012**, *55*, 2598–2610. [CrossRef]
30. Sharov, A.I.; Gutjahr, K.; Pellikka, P.E. Phase gradient approach to the evaluation and mapping of glacier rheology from multi-pass SAR interferograms. In *Analysis of Multi-Temporal Remote Sensing Images*; World Scientific Publishing: Singapore, 2004; pp. 154–165. [CrossRef]
31. Wang, J. Theory and methodology for landslide remote sensing and remote survey prediction. *Acta Geod. Cartogr. Sin.* **2007**, *4*, 369.
32. Liu, Z.M.; Wang, T. High-resolution interseismic strain mapping from InSAR phase-gradient stacking: Application to the North Anatolian Fault with implications for the non-uniform strain distribution related to coseismic slip distribution. *Geophys. Res. Lett.* **2023**, *50*, e2023GL104168. [CrossRef]
33. Fu, L.; Zhang, Q.; Wang, T.; Li, W.; Xu, Q.; Ge, D. Detecting slow-moving landslides using InSAR phase-gradient stacking and deep-learning network. *Front. Environ. Sci.* **2022**, *10*, 963322. [CrossRef]
34. Wang, G.X. Key technique in landslide control and its handling measures. *Chin. J. Rock. Mech. Eng.* **2005**, *24*, 20–29.
35. Xu, Q.; Guo, C.; Dong, X.; Li, W.; Lu, H.; Fu, H.; Liu, X. Mapping and characterizing displacements of landslides with InSAR and airborne LiDAR technologies: A case study of Danba County, southwest China. *Remote Sens.* **2021**, *13*, 4234. [CrossRef]
36. Zhang, C.; Li, Z.; Yu, C.; Chen, B.; Ding, M.; Zhu, W.; Yang, J.; Liu, Z.; Peng, J. An integrated framework for wide-area active landslide detection with InSAR observations and SAR pixel offsets. *Landslides* **2022**, *19*, 123–135. [CrossRef]
37. Cao, D.D. Spatial and temporal characteristics of the deformation field of landslide mass based on displacements and strain fields. *Geod. Geodyn.* **2023**, *43*, 498–504. [CrossRef]
38. Zhang, D.; Zhang, L.; Dong, J.; Wang, Y.; Yang, C.; Liao, M. Improved phase gradient stacking for landslide detection. *Landslides* **2024**, *21*, 1829–1847. [CrossRef]
39. Zhu, Z.R.; Li, X.T.; Wu, X.L. Study on spatio-temporal deformation characteristics of landslides based on strain analysis. *J. Geodesy Geodyn.* **2025**, *45*, 1–9. [CrossRef]
40. Ran, Q.F.; Jiang, Z.M. Application of landslide sensors and inclinometers in slope monitoring of Xiaolongtan Coal Mine. *Open Pit. Min. Technol.* **1990**, *4*, 22–25.
41. Ran, H.Q.; Zhang, J.C.; Xie, W.W.; Zhang, Y.J.; Song, Z.M.; Xiang, J.W.; Liu, J.H.; Feng, Q.Z.; Yan, T.N.; Jia, M.L.; et al. Applications study of geo-drilling technology. *Acta Geol. Sin.* **2011**, *85*, 1806–1822.
42. Wang, D.; Li, Y.; Zhou, H.J.; Liu, Y.J.; Zhang, L.X.; Sun, J.H. Analysis on present situation of geological drilling in China and the development prospects. *Explor. Eng. (Rock Soil Drill. Tunneling)* **2016**, *43*, 1–9.
43. Liu, X.H. Safety monitoring methods and evaluation theories for slope stability. In *Proceedings of the 2018 Annual Academic Exchange Conference of Yunnan Provincial Hydraulic Society*; Shuifu County Water Authority: Shuifu County, China, 2018; pp. 487–530.
44. Zhu, H.H.; Shi, B.; Yan, J.F.; Chen, C.; Li, Y.; Wang, J.; Zhang, J. Physical model testing of slope stability based on distributed fiber-optic strain sensing technology. *Chin. J. Rock. Mech. Eng.* **2013**, *32*, 821–828.
45. Qiu, Z.H. On monitoring precursors of major earthquakes with dense network of borehole strainmeters. *Acta Seismol. Sin.* **2014**, *36*, 738–749.
46. Shi, J.S.; Shi, L.; Wu, S.R. Difficulties and problematical aspects of landslide risk assessment: An overview. *Geol. Rev.* **2007**, *53*, 797–806.
47. Xu, X.Y.; Zhu, H.H.; Zhang, W.; Zhang, C.C.; Shi, B. Development of fiber optic monitoring-based visualization system for strain fields of slopes. *Chin. J. Geotech. Eng.* **2017**, *39*, 96–100. [CrossRef]
48. Hu, R.L.; Fan, L.F.; Wang, S.S.; Yu, Z.H.; Wang, X.L. Theory and method for landslide risk assessment—Current status and future development. *J. Eng. Geol.* **2013**, *21*, 76–84.
49. Price, E.J.; Sandwell, D.T. Small-scale deformations associated with the 1992 Landers, California, earthquake mapped by synthetic aperture radar interferometry phase gradients. *J. Geophys. Res. Solid Earth* **1998**, *103*, 27001–27016. [CrossRef]
50. Guo, L.M. Acquisition and application of three-dimensional deformation fields based on InSAR and multi-source data. *Recent. Dev. World Seismol.* **2015**, *8*, 40–42.

51. Hu, J.; Li, Z.W.; Zhu, J.J.; Ren, X.Z.; Ding, X.L. Inferring three-dimensional surface displacement field by combining SAR interferometric phase and amplitude information of ascending and descending orbits. *Sci. China Earth Sci.* **2010**, *40*, 307–318. [CrossRef]
52. Hu, J. Theory and Method of Estimating Three-Dimensional Displacement with InSAR Based on the Modern Surveying Adjustment. Ph.D. Thesis, Central South University, Changsha, China, 2013.
53. Berardino, P.; Fornaro, G.; Lanari, R.; Sansosti, E. A new algorithm for surface deformation monitoring based on small baseline differential SAR interferograms. *IEEE Trans. Geosci. Remote Sens.* **2002**, *40*, 2375–2383. [CrossRef]
54. Sandwell, D.T.; Price, E.J. Phase gradient approach to stacking interferograms. *J. Geophys. Res. Solid. Earth* **1998**, *103*, 30183–30204. [CrossRef]
55. Hooper, A. A multi-temporal InSAR method incorporating both persistent scatterer and small baseline approaches. *Geophys. Res. Lett.* **2008**, *35*, L16302. [CrossRef]
56. Xu, C.J. *Crustal Deformation Measurement and Data Processing*; Wuhan University Press: Wuhan, China, 2010; ISBN 978-7-307-07176-6.
57. Ding, Y. Study on the Stability of High Loess Slope Under Artificial Rainfall Simulation. Master's Thesis, Northwest University, Xi'an, China, 2011.
58. Liu, Z.X.; Zhao, G.M.; Meng, X.R.; Gu, Q.H.; Qin, Z.H. Study on aging characteristics of creep strain energy density evolution and damage constitutive model of rock. *J. Mining Strata Control Eng.* **2025**, *7*, 157–170. [CrossRef]

Disclaimer/Publisher's Note: The statements, opinions and data contained in all publications are solely those of the individual author(s) and contributor(s) and not of MDPI and/or the editor(s). MDPI and/or the editor(s) disclaim responsibility for any injury to people or property resulting from any ideas, methods, instructions or products referred to in the content.